

# Anomalous Change Point Detection Using Probabilistic Predictive Coding

Roelof G. Hup<sup>1</sup>, Julian P. Merkofer<sup>1\*</sup>, Alex A. Bhogal<sup>2</sup>,  
Ruud J.G. van Sloun<sup>1</sup>, Reinder Haakma<sup>3</sup>, Rik Vullings<sup>1</sup>

<sup>1</sup>Department of Electrical Engineering, Eindhoven University of Technology, Eindhoven, The Netherlands.

<sup>2</sup>Translational Neuroimaging Group, Center for Image Sciences, University Medical Center Utrecht, Utrecht, The Netherlands.

<sup>3</sup>Department of Patient Care & Monitoring, Philips Research, Koninklijke Philips N.V., Eindhoven, The Netherlands.

\*Corresponding author(s). E-mail(s): [j.p.merkofer@tue.nl](mailto:j.p.merkofer@tue.nl);

Contributing authors: [r.g.hup@tue.nl](mailto:r.g.hup@tue.nl); [a.bhogal@umcutrecht.nl](mailto:a.bhogal@umcutrecht.nl);  
[r.j.g.v.sloun@tue.nl](mailto:r.j.g.v.sloun@tue.nl); [reinder.haakma@philips.com](mailto:reinder.haakma@philips.com); [r.vullings@tue.nl](mailto:r.vullings@tue.nl);

## Abstract

Change point detection (CPD) and anomaly detection (AD) are essential techniques in various fields to identify abrupt changes or abnormal data instances. However, existing methods are often constrained to univariate data, face scalability challenges with large datasets due to computational demands, and experience reduced performance with high-dimensional or intricate data, as well as hidden anomalies. Furthermore, they often lack interpretability and adaptability to domain-specific knowledge, which limits their versatility across different fields. In this work, we propose a deep learning-based CPD/AD method called Probabilistic Predictive Coding (PPC) that jointly learns to encode sequential data to low dimensional latent space representations and to predict the subsequent data representations as well as the corresponding prediction uncertainties. The model parameters are optimized with maximum likelihood estimation by comparing these predictions with the true encodings. At the time of application, the true and predicted encodings are used to determine the probability of conformity, an interpretable and meaningful anomaly score. Furthermore, our approach has linear time complexity, scalability issues are prevented, and the method can easily be adjusted to a wide range of data types and intricate applications. We demonstrate the effectiveness and adaptability of our proposed method across

synthetic time series experiments, image data, and real-world magnetic resonance spectroscopic imaging data.

**Keywords:** change point detection, anomaly detection, predictability modeling, deep learning

## 1 Introduction

Change point detection (CPD) and anomaly detection (AD) are critical techniques in various fields, involving the detection of abrupt changes or abnormal instances in sequential data, respectively. Both techniques are widely used in finance surveillance and fraud detection (Hilal, Gadsden, & Yawney, 2022), Internet of Things and (remote) health monitoring (Fahim & Sillitti, 2019), video surveillance (Duong, Le, & Hoang, 2023), and intrusion detection in cyber security systems (Z. Yang et al., 2022). With ever-increasing amounts of data, these techniques have become more important, as they decrease labor efforts and enable the detection of subtle but significant anomalies and change points.

When the objective is to detect anomalous change points, the fields of CPD and AD intersect, in the sense that change points can be either normal or anomalous. For example, in the field of computer vision and video surveillance, changes in image contrast or brightness are generally not anomalous, while substantial changes may be anomalous (Theiler & Perkins, 2006). Similarly, in fields like water resource management (Apostol, Truică, Pop, & Esposito, 2021) and hardware Trojan detection (Elnaggar, Chakrabarty, & Tahoori, 2019), failing to consider the existence of normal change points in anomaly detection leads to numerous false alarms, as routine changes may trigger unnecessary alerts.

Despite the importance of CPD and AD, existing methods often encounter significant limitations. These include constraints on data types, such as being applicable only to univariate data, scalability issues with large datasets due to high computational complexity, and performance degradation with high-dimensional, complex data, or concealed anomalies. Moreover, many methods lack interpretability, fail to provide meaningful scores, cannot be tuned to domain knowledge, or are overly specialized in particular domains, hindering their cross-domain applicability. These limitations are further discussed in section 2.

In this work, we propose Probabilistic Predictive Coding (PPC), a method that does not suffer from these limitations. PPC is a deep learning-based CPD/AD method that encodes sequential data to latent space representations and thus can be adapted to a wide range of data types, including time series, images, videos, graphs, sets, and text data. Due to the application of deep learning, the computational complexity at application time is linear to the number of samples, preventing scalability issues. At the same time, the deep learning approach makes the method widely applicable in different domains with different levels of data complexity, while still being able to be tuned to domain knowledge. By using predictability modeling, the method is intuitive

and interpretable. Furthermore, due to its probabilistic nature, the method can provide a meaningful anomaly score in the form of a *probability of conformance*.

## 2 Background

### 2.1 Applications of CPD and AD

In this section, we provide a non-exhaustive list of applications of change point detection and anomaly detection.

**Financial surveillance:** In the financial sector, financial fraud detection systems for credit card fraud, insurance fraud, money laundering, healthcare fraud, and securities and commodities fraud have gained interest due to increasing incidence rates. In the US alone, yearly costs associated with financial fraud are estimated to accumulate to over \$400 billion (Hilal et al., 2022). We refer the reader to an extensive review on this topic by Hilal et al. (2022).

**Sensor monitoring:** Due to the advancement of sensor monitoring technologies within physical spaces and objects, e.g., inhabitant environments, transportation systems, health care systems, and industrial systems, the need for automated analysis of large data streams has become apparent. Timely detection of malfunctioning equipment may prevent unexpected problems (Fahim & Sillitti, 2019). The work of Fahim and Sillitti (2019) provides a literature review on this topic.

**Video surveillance:** With an increasing demand for public security, the use of surveillance cameras for crime prevention and counter-terrorism has risen. However, manual human monitoring is labor-intensive, especially given the low incidence rate of abnormal events. In the field of video surveillance, anomaly detection for automated monitoring is an active area of research (Duong et al., 2023). We refer the reader to a survey for deep learning-based video surveillance approaches by Duong et al. (2023).

**Cyber security systems:** For decades, anomaly detection systems have been used to monitor network traffic in computer systems for malicious requests. Research into intrusion detection systems (IDS) has been active, especially within the machine learning community (Z. Yang et al., 2022). The work of Z. Yang et al. (2022) contains a systematic literature review on this topic.

### 2.2 Review of existing methodologies

Most surveys on anomaly detection make a clear distinction between conventional/classical/traditional methods and deep learning-based methods. As identified by Pang, Shen, Cao, and Hengel (2022), previous surveys tend to focus on conventional methods, while the research field of *deep anomaly detection* is very active. In this section, we will provide a short survey of existing classical and deep learning-based methods, including relevant strengths and weaknesses.

### 2.2.1 Classical methods

Recently, [Samariya and Thakkar \(2023\)](#) surveyed traditional anomaly detection methods, where they sorted these algorithms into several categories. We refer the reader to this work for extensive information on this topic but will summarize the categories.

Statistical models like Grubbs’s test ([Grubbs, 1969](#)) or  $\chi^2$ -statistics ([N. Ye & Chen, 2001](#)) use statistical tests to find anomalies and provide statistically meaningful scores. Non-parametric statistical methods like histogram-based methods, e.g., [Gebski and Wong \(2007\)](#), and kernel-based algorithms such as proposed by [F. Liu, Yu, Song, Fan, and Tong \(2020\)](#), both apply a form of density estimation, assuming that anomalies have low density. While these methods are simple and intuitive, they have difficulties processing highly complex data.

Another density-based method is Local Outlier Factor (LOF) ([Breunig, Kriegel, Ng, & Sander, 2000](#)), which calculates the relative density of data instances with respect to their neighboring data instances. A high number of variants on LOF have been proposed, such as Resolution-based Outlier Factor (ROF) ([Fan, Zaïane, Foss, & Wu, 2009](#)), Global-Local Outlier Scores from Hierarchies (GLOSH) ([Campello, Moulavi, Zimek, & Sander, 2015](#)) and Simple univariate Probabilistic Anomaly Detector (SPAD) ([Aryal, Ting, & Haffari, 2016](#)). While these methods generally perform well, they are computationally expensive and are not suitable for large or high-dimensional datasets.

Distance-based methods assume that anomalous data instances lie far away from their nearest neighbors. Well-known examples are the k-nearest neighbors algorithm ([Knorr, Ng, & Tucakov, 2000](#)) and AntiHub ([Radovanovic, Nanopoulos, & Ivanovic, 2015](#)). These methods are relatively easy to implement but are computationally expensive, less effective in large or high-dimensional datasets, and do not provide intuitive anomaly scores.

Clustering-based methods assume that anomalous data instances are not part of a cluster of data instances. By clustering a collection of data instances, outliers can be detected. Examples of methods are OFP (Outlier Finding Process) ([M. Jiang, Tseng, & Su, 2001](#)) and Clustering-based Outlier Detection (CBOD) ([S.-y. Jiang & An, 2008](#)). These methods are adaptable to different data types and intricate problem setups. However, the performance of these types of methods is generally sensitive to the type of clustering algorithm and hyperparameters used, and in general, clustering is computationally expensive.

Isolation-based algorithms assume that anomalous data instances are easier to isolate than normal data instances when splitting data into partitions. Common methods are isolation forests ([F.T. Liu, Ting, & Zhou, 2012](#)) and Unsupervised Stochastic Forest-based Anomaly Detector (usfAD) ([Aryal, Santosh, & Dazeley, 2021](#)). While these methods have relatively low computational complexity compared to clustering- or distance-based methods, they do not provide meaningful or intuitive anomaly scores, as the scores lack context and are not normalized or standardized.

Lastly, subspace-based methods assume that anomalous data instances are hidden in a subset of features. By selecting a subspace and computing a score for that subspace, anomalies may be detected. Examples of such methods are Subspace Outlier Degree (SOD) ([Kriegel, Kröger, Schubert, & Zimek, 2009](#)) and Zero++ ([Pang, Ting,](#)

Albrecht, & Jin, 2016). While these methods are generally well able to detect anomalies concealed in high-dimensional spaces, they have high computational costs, similar to distance- and density-based methods.

### 2.2.2 Deep learning-based methods

In the recent work of Pang et al. (2022), the authors proposed a taxonomy for deep anomaly detection techniques, consisting of three main categories of techniques. The main difference between these categories is the degree to which the anomaly score is part of the model training pipeline. We refer the reader to this work for more details but will summarize this taxonomy and give the advantages and disadvantages of current approaches.

Whenever the anomaly scoring mechanism and the deep learning model are independently established, the authors refer to *deep learning for feature extraction*. The main objective is to apply nonlinear dimensionality reduction instead of more traditional linear methods like principal component analysis (PCA). In that sense, deep learning techniques have been shown to extract significantly richer features (Goodfellow, Bengio, & Courville, 2016), which can subsequently be used with any of the classical methods mentioned in section 2.2.1. While these methods are generally easy to implement and pre-trained deep learning models are widely available, disjoint development of the feature extraction and anomaly scoring mechanisms often leads to sub-optimal performance (Pang et al., 2022).

On the other end of the spectrum, *end-to-end anomaly score training* aims to fully include the anomaly score in the training pipeline. No existing or pre-defined anomaly measures are needed with this approach, as the network itself has to learn the anomaly scores directly. Examples within this category include ranking models (e.g., LeSiNN, Pang, Ting, and Albrecht (2015)), prior-driven models (e.g., Oh and Iyengar (2019)), softmax likelihood models (e.g., Chen, Tang, Sun, Chen, and Zhang (2016)), and end-to-end one-class classification methods (e.g., Sabokrou, Khalooei, Fathy, and Adeli (2018)). One major advantage of these methods is that direct optimization of the anomaly scores is possible, often leading to great performance. However, they generally require weak supervision and some form of labeled anomalies. Furthermore, providing these labeled anomalies may inhibit generalization to unseen anomalies.

The last proposed category is somewhere in between the previous two categories. It aims to learn feature representations of non-anomalous data instances, hence the name *learning feature representations of normality*. Some examples of generic methods that capture data regularities are autoencoders (e.g., variational autoencoders, Doersch (2016)), generative adversarial networks (e.g., f-AnoGAN (Schlegl, Seeböck, Waldstein, Langs, & Schmidt-Erfurth, 2019)), predictability modeling (e.g., AnoPCN (M. Ye, Peng, Gan, Wu, & Qiao, 2019)), and self-supervised classification methods (e.g., Tenenboim-Chekina, Rokach, and Shapira (2013)). Additionally, some methods are specifically tuned to certain anomaly measures, such as distance-based measures (e.g., Wang, Pang, Shen, and Ma (2020)), one-class classification measures (e.g., Wu, Liu, and Shen (2019)), and clustering-based measures (e.g., X. Yang, Deng, Zheng, Yan, and Liu (2019)). Most of these methods are easy to implement and only require

semi-supervised training with non-anomalous data. However, these methods generally lack clear interpretability, provide anomaly scores without sufficient contextual information or a standardized scale, or are computationally complex and expensive.

Closest to our proposed method is the VAE-LSTM method introduced by Lin et al. (2020), falling in the category *learning feature representations of normality*. VAE-LSTM uses a hybrid method consisting of variational autoencoders (VAE) and long short-term memory (LSTM) to detect anomalies. Similar to PPC, it aims to encode data to latent space representations and predict future representations using the LSTM. However, the VAE and LSTM models are trained disjointly, which yields latent space representations that are not optimized for prediction purposes (Pang et al., 2022). In our method, we jointly train the encoder model and prediction models to enhance the anomaly detection performance. Furthermore, VAE-LSTM uses a decoder to reconstruct the original data instances based on the (predicted) latent space representations, where the reconstruction error is used as the anomaly score. We opted to calculate a more meaningful and intuitive anomaly score by obtaining probabilistic predictions of latent space representations and comparing them with the true representations, yielding a probability of conformance.

## 3 Methods

### 3.1 Problem definition

Let  $\{x_1, x_2, \dots\}$  be a set consisting of data instances of any type that are *sequential*, *predictable*, and *encodable*. Data instances are sequential whenever they are part of a unidirectional succession, e.g.,  $x_2$  succeeds  $x_1$ ,  $x_3$  succeeds  $x_2$ , etc. The property of predictability is applicable whenever individual data instances can be reasonably estimated given prior data instances in the sequence, indicated by a relatively high entropy of the conditional probability density function  $f(x_{j+i}|x_1, x_2, \dots, x_j)$  for prediction step  $i$ . Data instances are encodable whenever all data instances  $\{x_1, x_2, \dots\}$  can be transformed to low-dimensional latent space representations  $\{z_1, z_2, \dots\}$  with an encoder neural network, and these latent space representations contain the necessary information to satisfy the requirement of predictability. Obvious examples of data that meet these requirements are video (e.g., with convolutional neural networks) or text (e.g., with Word2vec), but certain time series, images, and even graphs may qualify as well. It is up to the user to define a sequential axis within the data such that the data instances indeed have these properties.

Based on these properties, we propose a method that is able to encode sequential data instances into a latent space representation and make predictions of the next latent space representations in the sequence. In this way, highly intricate data can be reduced in complexity and predicted representations can be compared to the actual representations, giving us a proxy of the likelihood function  $f(x_{j+i}|x_1, x_2, \dots, x_j)$  and therefore a measure to determine whether the actual data instance was expected or likely. Within the taxonomy proposed by Pang et al. (2022), this method would be considered as *predictability modeling*, where the latent space representations of non-anomalous data instances are learned in a semi-supervised manner.

### 3.2 Probabilistic predictions

The objective of the proposed method is to encode a set of  $N_p$  data instances  $\{x_1, x_2, \dots, x_{N_p}\}$  to their corresponding latent space representations  $\{z_1, z_2, \dots, z_{N_p}\}$  and use these to predict the distribution(s) of the subsequent representation(s)  $\{\hat{z}_{N_p+1}, \hat{z}_{N_p+2}, \dots\}$  and the corresponding prediction uncertainty  $\{\sigma_{N_p+1}, \sigma_{N_p+2}, \dots\}$ . Without loss of generality, we let  $z_{N_p+i}, \hat{z}_{N_p+i} \in \mathbb{R}^{N_e}, \sigma_{N_p+i} \in \mathbb{R}_{>0}^{N_e}$  for prediction step  $i$  and assume that the prediction error is distributed according to a multivariate normal distribution with zero covariance, i.e.,  $Z_{N_p+i} \sim \mathcal{N}(\hat{z}_{N_p+i}, \text{diag}(\sigma_{N_p+i}^2))$ . Note that other continuous and differentiable probability distributions could be used as well. Discrete probability distributions could potentially be used using the Gumbel-Softmax reparameterization trick (Huijben, Kool, Paulus, & van Sloun, 2023; E. Jang, Gu, & Poole, 2017).

Now, to encode the data instances and predict latent space representations of the next data instances in the sequence, we adapted the Contrastive Predictive Coding pipeline (CPC) proposed by Oord, Li, and Vinyals (2018). While CPC is originally used for representation learning, the authors demonstrated its ability to learn high-quality representations combined with its predictive abilities, which forms a suitable basis for the objectives within the current work.

Similar to the CPC pipeline, our pipeline uses an encoder neural network  $E$  to encode the data instances into low-dimensional latent space encodings, i.e.,  $z_k = E(x_k)$ . A recurrent neural network  $G$  translates multiple sequential encodings to a context vector  $c_{N_p}$ , noted as  $c_{N_p} = G(z_1, z_2, \dots, z_{N_p})$ . This context vector then forms the basis for predictions of future latent space representations, where several forecasting neural networks  $F_1, F_2, \dots, F_{N_f}$  transform this context vector into predictions for the next  $N_f$  latent space representations, i.e.,  $(\hat{z}_{N_p+i}, \sigma_{N_p+i}) = F_i(c_{N_p})$ .

While CPC uses single-layer perceptrons without estimating prediction uncertainty, we opted to use mean-variance estimation neural networks that employ multi-task learning to estimate both the encoding  $\hat{z}_{N_p+i}$  and the associated prediction uncertainty  $\sigma_{N_p+i}$  (Nix & Weigend, 1994). We opted with the proposed PPC method for probabilistic predictions because (1) this allows for calculating a proxy of the likelihood  $f(x_{N_p+i}|x_1, x_2, \dots, x_{N_p})$  (see section 3.3), (2) this likelihood is an intuitive and non-arbitrary distance metric between ground truth and predicted encodings and forms a suitable loss function for training neural networks (see section 3.4), and (3) probabilistic predictions allow for a nuanced and statistically meaningful interpretation of the output in the form of a *probability of conformance* (see section 3.5). Figure 1 shows an example of the PPC pipeline architecture.

### 3.3 Tractable proxy for the density function

While the computation of  $f(x_{N_p+i}|x_1, x_2, \dots, x_{N_p})$  can be intractable in highly intricate and/or high-dimensional data, given the steps taken in the previous section, a proxy can be defined for this conditional probability density function. By applying maximum likelihood optimization to the pipeline, the encoding mechanism of model  $E$  and the predictive mechanism of models  $G$  and  $F_1, F_2, \dots, F_{N_f}$  are jointly and symbiotically optimized to create an ordered latent space, such that models  $G$

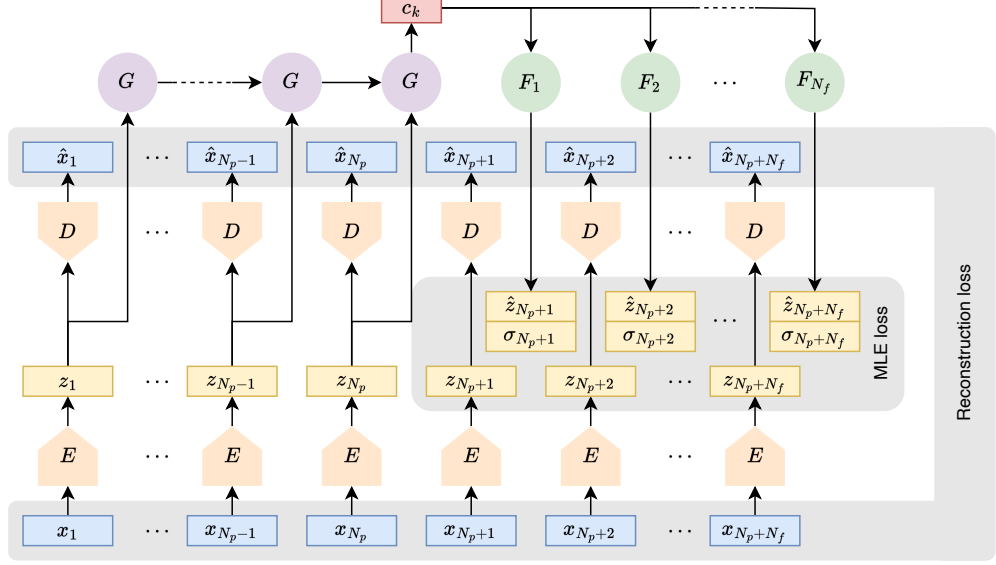


**Fig. 1** The PPC pipeline architecture. Encoder model  $E$  encodes data instances to their latent space representations, and decoder model  $D$  aims to reconstruct the original data instances. Recurrent neural network model  $G$  and forecasting models  $F_i$  make predictions of the latent space encodings of future latent space representations given the past data instances. Maximum likelihood estimation (MLE) loss and reconstruction loss are depicted in gray.

and  $F_1, F_2, \dots, F_{N_f}$ , given the latent space representations within this ordered latent space, yield accurate density estimates of future latent space representations  $z_{N_p+i}$ .

Whenever the models accurately capture the underlying conditional distribution  $f(x_{N_p+i} | x_1, x_2, \dots, x_{N_p})$ , this distribution should be reflected in the density estimates of  $z_{N_p+i}$ . As the data space and latent space generally differ in volume, we assume the relationship between these two density functions to be proportional, e.g.,

$$\begin{aligned}
 f(x_{N_p+i} | x_1, x_2, \dots, x_{N_p}) &\propto f(E(x_{N_p+i}) | F_i(G(E(x_1), E(x_2), \dots, E(x_{N_p})))) \\
 &= f(z_{N_p+i} | F_i(G(z_1, z_2, \dots, z_{N_p}))) \\
 &= f(z_{N_p+i} | \hat{z}_{N_p+i}, \sigma_{N_p+i}).
 \end{aligned} \tag{1}$$

In section 4.1, we will present an experiment for which this relationship holds, indicating that the pipeline indeed has the potential to estimate  $f(z_{N_p+i} | \hat{z}_{N_p+i}, \sigma_{N_p+i})$  as a suitable proxy for  $f(x_{N_p+i} | x_1, x_2, \dots, x_{N_p})$ .

Furthermore, as  $f(z_{N_p+i} | \hat{z}_{N_p+i}, \sigma_{N_p+i})$  takes the form of the density function of a multivariate normal distribution, i.e.,

$$f(z_{N_p+i} | \hat{z}_{N_p+i}, \sigma_{N_p+i}) = \prod_{n=1}^{N_e} \frac{1}{\sqrt{2\pi} \cdot (\sigma_{N_p+i})_n} \exp\left(-\frac{1}{2} \cdot \frac{[(z_{N_p+i})_n - (\hat{z}_{N_p+i})_n]^2}{(\sigma_{N_p+i})_n^2}\right), \tag{2}$$



it becomes clear that this proxy is tractable for both model training and application. Note that, for notation purposes,  $(\cdot)_n$  denotes the  $n$ th element in the vector.

### 3.4 Training procedure

While CPC uses InfoNCE loss (Oord et al., 2018), this contrastive loss function is not compatible with the probabilistic outputs of the forecasting models. Therefore, we opted for training the models  $E$ ,  $G$  and  $F_1, F_2, \dots, F_{N_f}$  with maximum log-likelihood estimation, yielding

$$\begin{aligned} \mathcal{L}_{\text{MLE}} &= -\frac{1}{N_f} \sum_{i=1}^{N_f} \log f(z_{N_p+i} | \hat{z}_{N_p+i}) \\ &= -\frac{1}{N_f} \sum_{i=1}^{N_f} \log \prod_{n=1}^{N_e} \frac{1}{\sqrt{2\pi} \cdot (\sigma_{N_p+i})_n} \exp\left(-\frac{1}{2} \cdot \frac{[(z_{N_p+i})_n - (\hat{z}_{N_p+i})_n]^2}{(\sigma_{N_p+i})_n^2}\right) \\ &= N_e \log(\sqrt{2\pi}) + \frac{1}{N_f} \sum_{i=1}^{N_f} \left( \sum_{n=1}^{N_e} \log(\sigma_{N_p+i})_n + \frac{1}{2} \sum_{n=1}^{N_e} \frac{[(z_{N_p+i})_n - (\hat{z}_{N_p+i})_n]^2}{(\sigma_{N_p+i})_n^2} \right), \end{aligned} \quad (3)$$

where  $N_e$  is the size of the latent space representation vector and zero covariance is assumed in the  $N_e$ -variate normally distributed predictions.

Recent work by Sluijterman, Cator, and Heskes (2023) has confirmed that mean-variance estimation neural networks benefit from a warm-up period in training where the variances are fixed and do not count toward the gradients within backpropagation, so we assumed  $\forall_n (\sigma_{k+i})_n = 1$ , reducing the MLE loss to

$$\mathcal{L}_{\text{MLE}} = N_e \log(\sqrt{2\pi}) + \frac{1}{2N_f} \sum_{i=1}^{N_f} \sum_{n=1}^{N_e} [(z_{N_p+i})_n - (\hat{z}_{N_p+i})_n]^2, \quad (4)$$

which corresponds to optimizing the mean squared error. This simplified loss function is used during the first training iterations, either for a fixed amount of iterations (e.g., 1000) or until convergence. After warm-up, the training continues with the full MLE loss.

Note that the current combination of the encoder model, recurrent neural network model, and forecasting models forms an underdetermined optimization problem, where the optimal set of model parameters would lead to the encoder always producing the same latent space representations, regardless of the encoder input, and the recurrent neural network and forecasting models always predicting those representations. In the original CPC work, the contrastive loss encouraged the encoder to produce different representations for the positive and negative samples, solving this problem of underdetermination.

As MLE does not use negative samples, we added a decoder model  $D$  to the pipeline with the sole task of reconstructing the original input  $x_k$  from the latent space representation  $z_k$ , yielding  $\hat{x}_k = D(z_k)$ . This form of regularization encourages the

encoder to produce meaningful representations. We chose the mean squared error as the additional loss term, yielding

$$\mathcal{L}_{\text{MSE}} = \frac{1}{N_p + N_f} \sum_{k=1}^{N_p + N_f} \text{MSE}(x_k, \hat{x}_k), \quad (5)$$

where MSE is the mean squared error function that is appropriate for the data type and dimensionality of the input sample  $x_k$ . Together with the MLE loss, this gives the optimization problem

$$\theta^* = \underset{\theta}{\text{argmin}} (\mathcal{L}_{\text{MLE}} + \lambda \cdot \mathcal{L}_{\text{MSE}}), \quad (6)$$

where  $\theta$  is the set of model parameters for models  $E$ ,  $G$ ,  $F_0$ ,  $F_1$ ,  $\dots$ ,  $F_{N_f}$ , and  $D$ , and  $\lambda$  is the weight assigned to the mean squared error. After training, the decoder  $D$  is no longer needed for the anomalous change point detection and can be discarded.

### 3.5 Probability of conformance

To determine whether the data element  $x_{N_p+i}$  was expected given  $x_1, x_2, \dots, x_{N_p}$ , we use the Mahalanobis distance  $d_M$  between  $\hat{z}_{N_p+i}$  and  $z_{N_p+i}$ ,

$$\begin{aligned} d_{z, N_p+i} &= d_M(z_{N_p+i}, \hat{z}_{N_p+i}, \sigma_{N_p+i}) \\ &= \sqrt{\sum_{n=1}^{N_e} \frac{[(z_{N_p+i})_n - (\hat{z}_{N_p+i})_n]^2}{(\sigma_{N_p+i})_n^2}}. \end{aligned} \quad (7)$$

Whenever we consider this distance as a function of  $Z_{N_p+i}$ , the distance becomes a random variable  $D_{z, N_p+i} = d_m(Z_{N_p+i}, \hat{z}_{N_p+i}, \sigma_{N_p+i})$ . Note that the squared Mahalanobis distance is a sum of squared independent univariate standard distributions, and therefore distributed according to a chi-squared distribution, i.e.,  $D_{z, N_p+i}^2 \sim \chi^2(N_e)$ .

Now, by using the corresponding cumulative distribution  $F_{D_{z, N_p+i}^2}$ , we can determine the probability of conformance in the latent space  $p_{z, N_p+i}$  with

$$\begin{aligned} p_{z, N_p+i} &= \text{P}\left(D_{z, N_p+i}^2 > d_{z, N_p+i}^2\right) \\ &= 1 - F_{D_{z, N_p+i}^2}\left(d_{z, N_p+i}^2, N_e\right). \end{aligned} \quad (8)$$

Note that in the case of  $N_e = 1$ , this reduces to

$$p_{z, N_p+i} = 2 \cdot Q\left(d_{z, N_p+i}^2\right), \quad (9)$$

where  $Q(\cdot)$  is the tail distribution function for a univariate standard distribution. The pipeline functions as a binary classifier whenever thresholding is applied to the probability of conformance in the latent space, i.e.,  $z_{N_p+i}$  is anomalous if  $p_{z, N_p+i} < \alpha$ .

In that case, the binary classifier rejects latent space representations with a probability of  $\alpha$ .

Now, if we consider the relationship with the probability of conformity in the data space,  $p_{x, N_p+i}$ , we must note that the relationship between  $f(z_{N_p+i}|\hat{z}_{N_p+i}, \sigma_{N_p+i})$  and  $p_{z, N_p+i}$  is strictly monotonically increasing. The same can trivially be said about the relationship between  $f(x_{N_p+i}|x_1, x_2, \dots, x_{N_p})$  and  $p_{x, N_p+i}$ . Due to the proportionality between  $f(z_{N_p+i}|\hat{z}_{N_p+i}, \sigma_{N_p+i})$  and  $f(x_{N_p+i}|x_1, x_2, \dots, x_{N_p})$  (see section 3.3), we can therefore conclude that the relationship between  $p_{z, N_p+i}$  and  $p_{x, N_p+i}$  is also strictly monotonically increasing. This indicates that the ordering of values of  $p_{x, N_p+i}$  is preserved in its proxy  $p_{z, N_p+i}$ , making this estimated probability of conformity in the latent space a useful metric for anomaly detection.

## 4 Experiments

### 4.1 Proportionality test

To determine whether the assumption of proportionality (see section 3.3), i.e.,  $f(x_{N_p+i}|x_1, x_2, \dots, x_{N_p}) = K \cdot f(z_{N_p+i}|\hat{z}_{N_p+i}, \sigma_{N_p+i})$  with constant  $K$ , holds, we conducted a relatively simple experiment with a well-defined data distribution. In this experiment,  $N_p = N_f = 1$ ,  $x_1 \in \{-10, 0, 10\}$ ,  $X_2 \sim \mathcal{N}(\mu_{X_2}(x_1), \sigma_{X_2}^2(x_1))$ ,  $\mu_{X_2}(x_1) = x_1$ , and  $\sigma_{X_2}(x_1) = 0.1 \cdot x_1 + 2$ . With this experiment, we challenged the pipeline to capture the data distributions for three different input data instances.

The pipeline consists of an encoder with a single fully connected layer to a latent space encoding with a size of  $N_e = 4$  and a decoder with a fully connected layer back to a single value. A gated recurrent unit (GRU) model with  $N_g = 8$  units is used for predictions together with a forecasting model consisting of 8 fully connected layers with [16, 16, 32, 32, 64, 64] units, followed by two separate fully connected layers for the estimation of  $\hat{z}_2$  (linear activation) and  $\sigma_2$  (exponential activation). Training is performed using the RMSprop optimizer ( $lr = 1 \cdot 10^{-4}$ ,  $\rho = 0.9$ ) with a batch size of 64. The models are optimized for 1000 warm-up iterations based on the loss in Equation 4, after which training with the normal loss function (Equation 3) continues until convergence. The loss weight for the reconstruction loss is set to  $\lambda = 100$ . Training is repeated 100 times to determine sensitivity to initial conditions, resulting in 100 models.

After training, each model was evaluated for every combination of values  $x_1 \in \{-10, 0, 10\}$  and  $x_2 \in [-16, 28]$ , where the range of  $x_2$  is chosen to allow evaluation of values of  $x_2$  within 6 standard deviations with respect to the ground truth data distribution means  $\mu_{X_2}(x_1) = x_1$ . The resulting probability functions were normalized to determine the probability density functions  $K \cdot f(z_{N_p+i}|\hat{z}_{N_p+i}, \sigma_{N_p+i})$ . Examples of the resulting functions are shown in Figure 2 with their corresponding ground truth data distributions. Considering that the shapes of Gaussian curves are sensitive to small deviations in parameters, we observe that the estimated PDFs tend to be similar to the ground truth data distributions.

To quantify the results, we fitted Gaussian functions to the obtained PDFs with zero residuals and compared the curve parameters  $\hat{\mu}_{X_2}$  and  $\hat{\sigma}_{X_2}$  to the ground truth

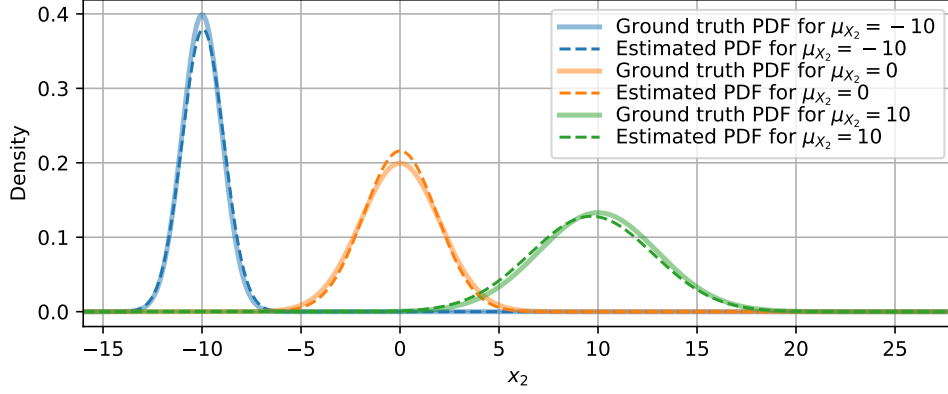


**Fig. 2** An example of ground truth and estimated probability distribution functions for three different values of  $x_1$ .

data distribution parameters  $\mu_{X_2}$  and  $\sigma_{X_2}$  for the different values of  $x_1$ . The mean and standard deviation of these Gaussian curve parameters are shown in Table 1.

**Table 1** Quantitative results of the proportionality test, consisting of true and estimated PDF parameters for different values of  $x_1$ .

$\mu_{X_2} = x_1$	$\sigma_{X_2}$	$\hat{\mu}_{X_2} (\mu \pm \sigma, N = 100)$	$\hat{\sigma}_{X_2} (\mu \pm \sigma, N = 100)$
-10	1	$-10.04 \pm 0.16$	$1.07 \pm 0.04$
0	2	$-0.02 \pm 0.13$	$1.84 \pm 0.06$
10	3	$9.66 \pm 0.19$	$3.11 \pm 0.10$

We can see that the ground truth and estimated parameters are almost identical in value, with relatively low standard deviations and thus low sensitivity to initial conditions. This indicates that the assumption of proportional probability density functions in the data and latent spaces holds.

## 4.2 Sine wave frequency deviation

As a first practical demonstration of the pipeline’s ability to detect anomalies, we synthesized a dataset of univariate signals in the form of (distorted) sine waves. The objective of the pipeline is to detect significant change points in sine wave frequency throughout the signal, where frequency-domain-based methods would not be able to.

To synthesize the appropriate training, validation and test datasets, we used a data-generating model  $s(t)$  that introduces small variations in instantaneous frequency, amplitude, and baseline, as well as additive noise. For every signal, a center frequency before ( $f_{c,before}$ ) and after the change point ( $f_{c,after}$ ) is chosen within the interval

[0.5, 10] Hz, resulting in the instantaneous frequency

$$f_c(t) = \begin{cases} f_{c,before} & \text{if } t \text{ before change point} \\ f_{c,after} & \text{if } t \text{ after change point} \end{cases}. \quad (10)$$

A signal containing the instantaneous frequencies at every time step  $f(t)$  is generated using a constrained random walk, such that  $f_c(t) - \frac{f_b}{2} \leq f(t) \leq f_c(t) + \frac{f_b}{2}$ , where  $f_b = 0.25$  Hz is the frequency band. Furthermore, bounded random walks were used to create a baseline wander  $-1 \leq b(t) \leq 1$  and wave amplitude  $0.5 \leq a(t) \leq 2$ . Lastly, additive noise was  $n(t) \sim \mathcal{N}(0, \sigma_n^2)$ , where  $\sigma_n \in [0, 0.2]$ . The corresponding sine wave signal was then determined by

$$s(t) = a(t) \cdot \sin\left(2\pi \int_0^t f(t) dt\right) + b(t) + n(t). \quad (11)$$

Using this data model, we synthesized a training and validation dataset of 1,000,000 and 100,000 signals respectively at a sampling frequency of  $f_s = 128$  Hz. The signals consist of 8 segments of 256 samples each, totaling 2048 samples (16 seconds). The first 5 segments  $x_1$  to  $x_5$  are used to predict the latent space representations of the last 3 segments  $x_6$  to  $x_8$ . The center frequencies were set such that  $f_{c,before} = f_{c,after}$ , implying the absence of change points. At the top of Figure 3, an example of such a non-anomalous signal is shown.

We used an encoder model  $E$  with two blocks (convolutional, ReLU, BatchNorm, Maxpooling) with an increasing amount of filters (32 and 64), followed by a fully connected layer to a latent space with size  $N_e = 16$ . The accompanying decoder  $D$  follows a similar structure with a fully connected layer, followed by two blocks (convolutional, ReLU, upsampling) and one final convolutional layer. As the recurrent neural network  $G$ , we used a GRU with 32 units. The three forecasting models  $F_1$ ,  $F_2$ , and  $F_3$  consist of three fully connected layers (64, 128, and 256 units), followed by two separate fully connected layers for the estimation of  $\hat{z}_6$  to  $\hat{z}_8$  (linear activation) and  $\sigma_6$  to  $\sigma_8$  (exponential activation). All models were optimized simultaneously using the RMSprop optimizer with a learning rate of  $1 \cdot 10^{-4}$  and a batch size of 32. Training consisted of 1000 warm-up iterations, followed by normal training until convergence. The reconstruction loss weight was set to  $\lambda = 10^4$ .

After training, the pipeline was applied to the test dataset, which was generated in a similar manner as the training and validation set, except that a change point was introduced in segment  $x_6$ . We generated the test dataset by synthesizing 10 signals for every combination  $(f_{c,before}, f_{c,after})$ , with a resolution of 0.05 Hz. This results in  $\left(\frac{10-0.5}{0.05}\right)^2 \cdot 10 = 361,000$  test signals. In the center and lower plots of Figure 3, some example signals are shown that have such a sudden change point.

Based on this test set, we calculated the log-likelihood and probability of conformance for every pair of center frequencies  $(f_{c,before}, f_{c,after})$ . These metrics were averaged and are shown in Figure 4, together with the frequency band with which the training and validation signals were generated. As expected, the probability of

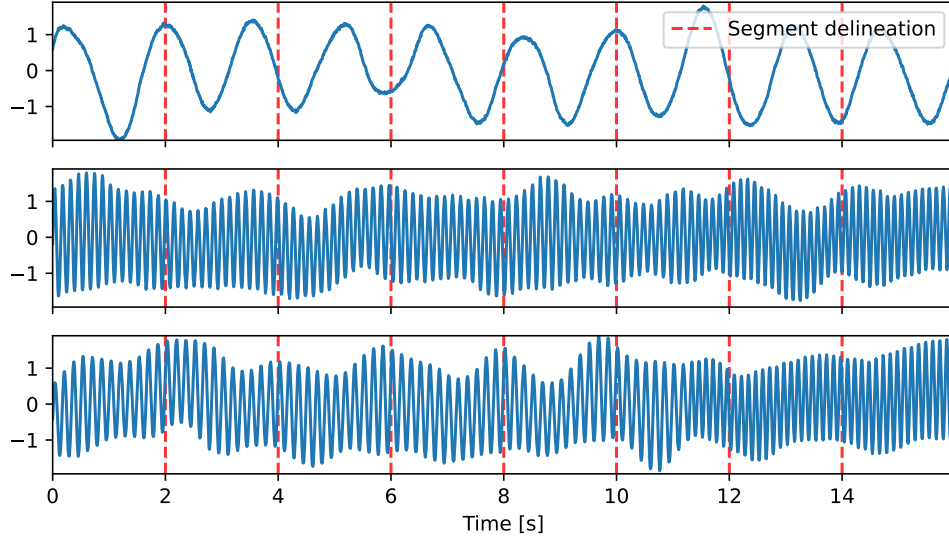


**Fig. 3** Examples of generated signals. The top signal has no frequency deviation. The center signal has a frequency change of 1 Hz at the change point around  $t = 11$  s. The bottom signal has a frequency change of 2 Hz at the change point around  $t = 11$  s.

conformance is high if  $f_{c,before} \approx f_{c,after}$ , and low for other combinations of center frequencies. This indicates that the model is able to detect the generated change points.

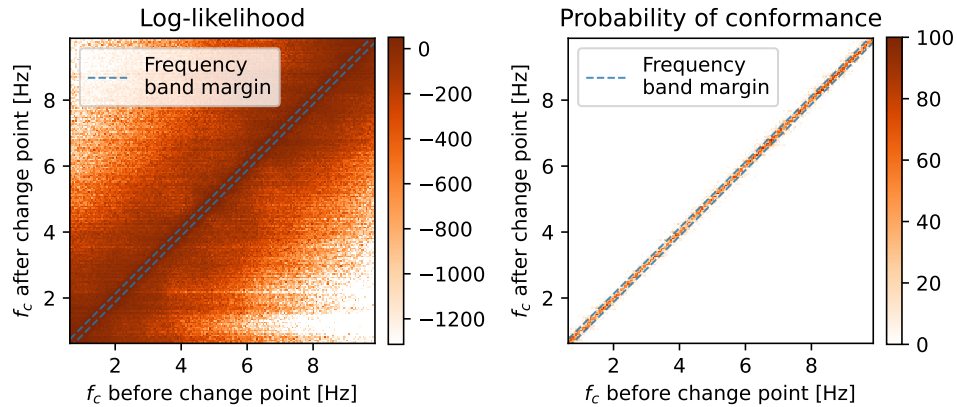


**Fig. 4** Average log-likelihood (left) and probability of conformity (right) per combination of center frequencies. The frequency band margins indicate how much frequencies may fluctuate as part of the generated instantaneous frequencies  $f(t)$ .

To test the discriminative performance of the pipeline, i.e., the ability of the pipeline to detect a sudden significant change in center frequency, we labeled all pairs  $(f_{c,before}, f_{c,after})$  where  $f_{c,before} = f_{c,after}$  as being true, and other pairs as false. We constructed the receiver operating characteristic (ROC) curve (see Figure 5) and

determined the area under the ROC curve (AUC) to be  $AUC = 0.99$ , indicating that the pipeline has a strong discriminative ability.

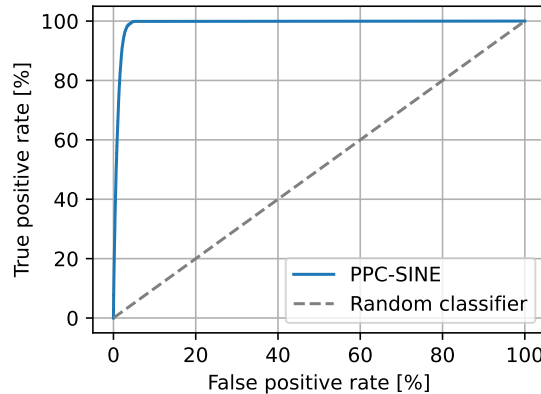


**Fig. 5** Receiver operating characteristic curve for the application of the PPC pipeline on the sine wave frequency deviation example.

### 4.3 Counting with MNIST digits

In this experiment, we used the Modified National Institute of Standards and Technology (MNIST) dataset (Lecun, Bottou, Bengio, & Haffner, 1998), consisting of 60,000 training images and 10,000 test images of handwritten digits. The objective within this experiment for the pipeline is to determine whether the corresponding digits of a set of two MNIST images are sequential, e.g., if  $x_1$  formed an image of the digit 3,  $x_2$  should represent the digit 4. In the special case of digit 9, we considered 0 to be its successor. The experiment was designed to determine if the pipeline is able to capture (deviations from) patterns in relatively complex sequential image data.

First, 10,000 validation images were selected from the original set of training images, reflecting the class composition of the training set. All image pixels were normalized to the range  $[0, 1]$ . Data augmentation is applied online, consisting of random rotation (between  $-18^\circ$  and  $18^\circ$ ), random rectangular zooming (between  $-5\%$  and  $5\%$ ), and random translation (between  $-5\%$  and  $5\%$ ).

We used an encoder model  $E$  with two blocks (convolutional, ReLU, BatchNorm, Maxpooling) with an increasing amount of filters (32 and 64), followed by a fully connected layer to a latent space with size  $N_e = 16$ . The accompanying decoder  $D$  follows a similar structure with a fully connected layer, followed by two blocks (convolutional, ReLU, upsampling) and one final convolutional layer. As the recurrent neural network  $G$ , we used a GRU with 32 units. The single forecasting model  $F_1$  consists of three fully connected layers (64, 128, and 256 units), followed by two separate fully connected layers for the estimation of  $\hat{z}_2$  (linear activation) and  $\sigma_2$  (exponential activation). All models were optimized simultaneously using the RMSprop optimizer with a learning rate of  $1 \cdot 10^{-4}$  and a batch size of 32. Training consisted of 1000 warm-up iterations,

followed by normal training until convergence. The reconstruction loss weight was set to  $\lambda = 10^4$ .

After training, the pipeline was used to compare every pair of two images in the test set, yielding a log-likelihood and probability of conformance for every pair. These metrics were averaged over every pair of digits and are shown in Figure 6. As expected, the log-likelihoods and probabilities of conformity on the subdiagonal and top right are significantly higher than for other combinations of digits. This indicates that the model indeed is able to differentiate between successive digits and non-successive digits. Some combinations, like the combination for (3, 9), show higher values due to the similarity between digits, e.g., a handwritten 4 is similar in shape to the digit 9.

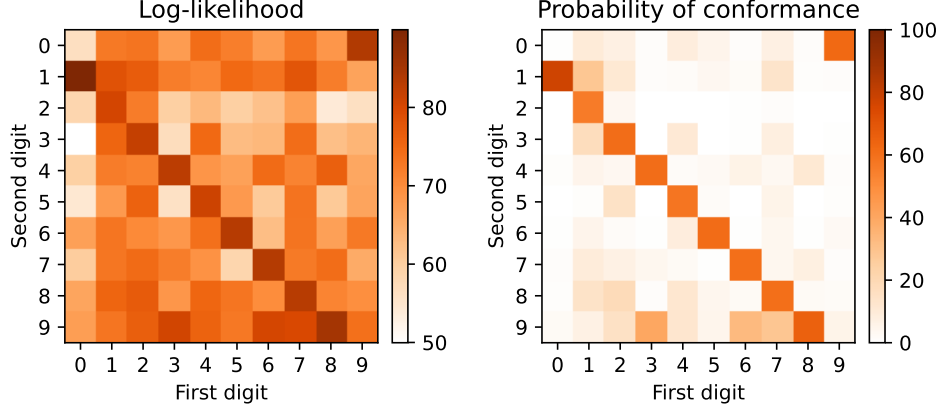


**Fig. 6** Average log-likelihood (left) and probability of conformity (right) per combination of digits.

To test the discriminative performance of the pipeline, i.e., the ability of the pipeline to determine whether a pair of digits is successive, we constructed the receiver operating characteristic (ROC) curve (see Figure 7) and determined the area under the ROC curve to be  $AUC = 0.95$ . Such a high AUC indicates that the pipeline has a strong discriminative ability.

Furthermore, to demonstrate the ability of the pipeline to learn latent space distributions, we applied principal component analysis (PCA) dimensionality reduction on the encodings of the test images to create 2D representations. We inferred the predicted distributions for each digit, reduced these distribution parameters to bivariate Gaussian distribution parameters using the same PCA model, and averaged the parameters over all inferred distributions.

In Figure 8, we show hexagonal binning plots for the reduced latent space representations for three example digits, and project the contours of the corresponding inferred bivariate distributions over these latent spaces. While PCA dimensionality reduction tends to remove essential information in the latent space, it can still be observed that the general shape of the distribution fits the shape of the hexagonal binning plots. This indicates that the pipeline is able to align the latent space and the predicted distributions, which is essential for anomalous change point detection.



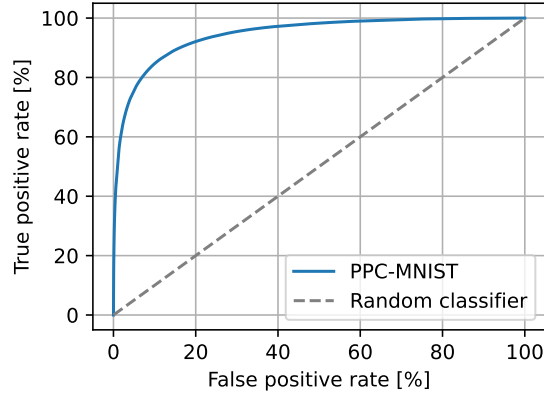


**Fig. 7** Receiver operating characteristic curve for the application of the PPC pipeline on the successive MNIST digits example.

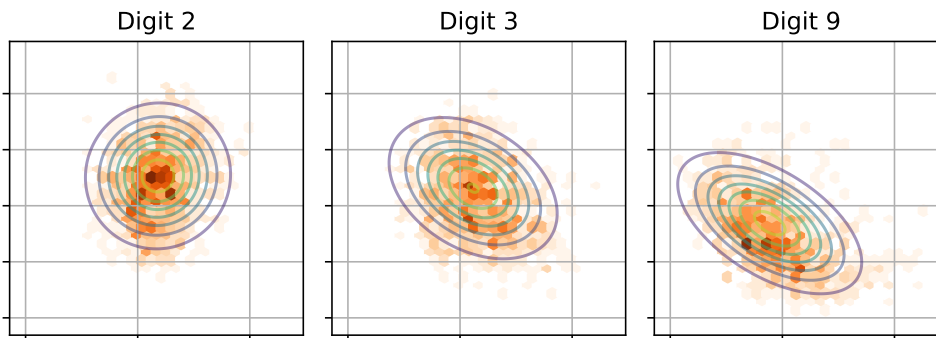


**Fig. 8** Hexagonal binning plots for the PCA-reduced latent space representations of different test images and digits, with contours of the inferred bivariate distributions projected over these plots.

#### 4.4 Artifact detection for MRSI

In this last experiment, we demonstrate the applicability of the proposed method to in-vivo proton magnetic resonance spectroscopic imaging (MRSI) data. MRSI allows non-invasive measurement and visualization of the chemical composition of tissues and has become a valuable tool for diagnosis and treatment monitoring of various diseases, such as cancer, neurological disorders, and traumatic brain injuries (Posse, Otazo, Dager, & Alger, 2013). However, clinical adoption of MRSI remains limited due to long acquisition times, low spatial resolutions, and variable spectral quality (Maudsley et al., 2021). Furthermore, the detection of artifacts is an active and challenging area of research (Kreis, 2004), specifically the automation thereof (Gurbani et al., 2018; J. Jang, Lee, Park, & Kim, 2021; Kyathanahally et al., 2018; Pedrosa de Barros, McKinley, Wiest, & Slotboom, 2017; van de Sande et al., 2023).

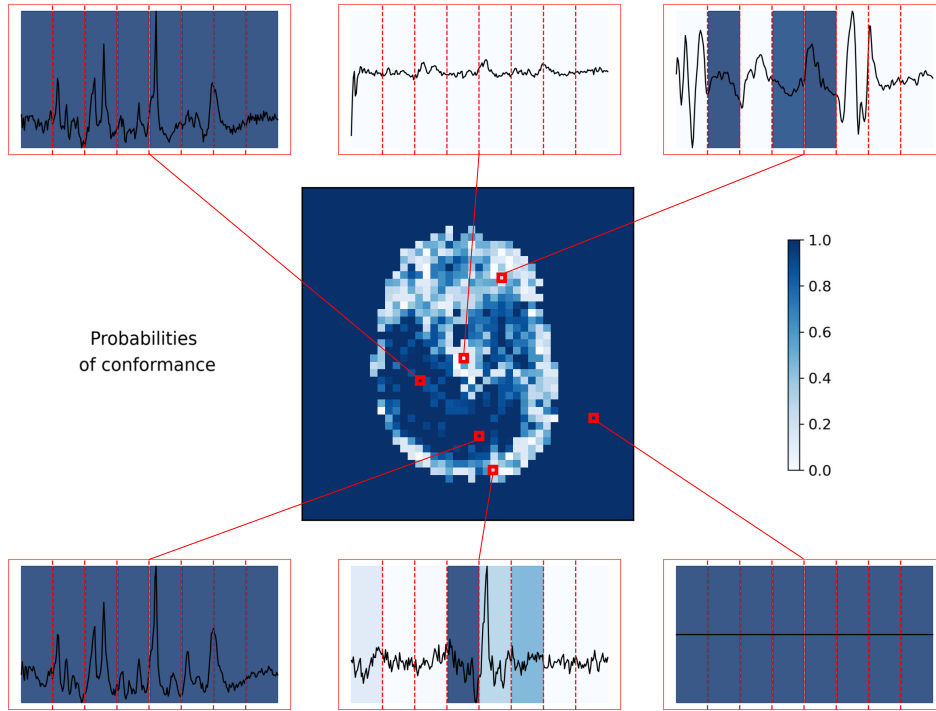
While metabolite signals and their characteristics are well understood and commonly modeled using density matrix simulations (Zhang, An, & Shen, 2017), other

signal contributions, like macromolecules, water/fat residuals, and other nuisance signals (Kreis, 2004) are anomalous due to sub-optimal localization performance and hardware imperfections (Kreis et al., 2021). Therefore, the proposed PPC pipeline was trained and validated with predictable synthetic single voxel spectroscopy (SVS) datasets and tested on in-vivo spectra of MRSI measurements. The simulated spectra were obtained using density matrix simulated metabolite signals with concentration ranges as reported for normal adult brains (De Graaf, 2019). To incorporate field inhomogeneities into the simulations, Lorentzian and Gaussian broadening were applied. In-vivo spectra were extracted from the MRSI database reported in Bhogal et al. (2020) as part of a study at the University Medical Center Utrecht. The data were acquired using a free-induction decay (FID) sequence at 7 Tesla with  $5 \times 5 \times 10$  mm sized voxels. Full data acquisition details are provided in the methods section of Bhogal et al. (2020).

The model takes a segment  $x_1$  (32 samples) of the SVS signal in the frequency domain and predicts the latent space representations of the next segment  $x_2$ . We used an encoder model  $E$  with four fully connected layers (512 units and ReLU activation), followed by a final linear layer to a latent space with size  $N_e = 16$ . The accompanying decoder  $D$  follows an identical structure with the final linear layer mapping back to the segment width. The recurrent neural network  $G$  consists of 32 units and the forecasting models  $F_1$  has 6 fully connected layers (64, 64, 128, 128, 256, and 256 units), followed by two separate fully connected layers for the estimation of  $\hat{z}_2$  (linear activation) and  $\sigma_2$  (exponential activation). All models were optimized simultaneously using the RMSprop optimizer with a learning rate of  $1 \cdot 10^{-4}$  and a batch size of 256. Training consisted of  $2 \cdot 10^4$  warm-up iterations, followed by normal training until convergence ( $2 \cdot 10^6$  iterations). The reconstruction loss weight was set to  $\lambda = 10^5$ .

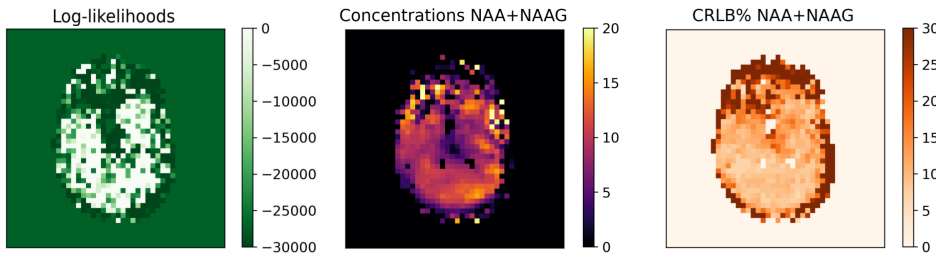
After training, the pipeline was used to predict all segments of every spectrum of an example in-vivo 2D MRSI slice. We further calculate the likelihoods and probabilities of conformance for every segment. Figure 9 depicts the probabilities of conformance for six example spectra located at the indicated locations as well as a probability map with pixels representing averaged spectra. Moving from the top left to top right spectrum: spectra within the homogeneous regions of the brain appear normal and show the highest probabilities of conformance, measurements near the ventricles are distorted completely, and susceptibility artifacts coming from the nasal cavity are present and detected by the method. From bottom left to right: non-anomalous spectra are consistently labeled with high probabilities, spectra close to the skull show residual lipid signal artifacts and lower probabilities of conformity, and the spectra outside the brain mask are nulled leading to no anomalies.

Figure 10 shows the estimated log-likelihoods next to the metabolite concentration map for total N-acetylaspartate (NAA + NAAG), one of the most prominent spectral components (Maudsley et al., 2021), as well as next to the obtained Cramér-Rao lower bound percentage values (CRLB%) for the metabolite concentration as estimated by the common quantification software LCModel (Provencher, 1993). The concentration estimates are obtained via least squares fitting of the measurements and a linear combination model of metabolite signals (Near et al., 2021). The CRLB% is calculated via the Fisher information matrix and represents a lower bound on the standard



**Fig. 9** In-vivo 2D MRSI slice with indicated locations of selected segmented example spectra. The probability of conformity is shown for each segment of the spectra as well as averaged for each pixel (representing a single voxel).

deviation of the estimates (Landheer & Juchem, 2021). It is commonly used as a quality measure for both SVS and MRSI (Kreis et al., 2021; Öz et al., 2014). Comparing the CRLB% with the estimated log-likelihoods and probabilities of conformance there is a clear inverse correlation, specifically concerning artifacts arising from the skull, the ventricles, and the nasal cavity.



**Fig. 10** 2D brain maps for the estimated likelihoods, the metabolite concentration map for total N-acetylaspartate (NAA + NAAG) estimated by LCModel (Provencher, 1993), as well as the corresponding CRLB% (left to right).

## 5 Discussion

In this work, we proposed a novel pipeline for anomalous change point detection that leverages the power of probabilistic predictions and latent space encoding to capture the underlying data distribution of non-anomalous data. Through several experiments, we demonstrated the effectiveness and wide applicability of our pipeline in detecting anomalous change points.

In contrast to some other methods mentioned in section 2, anomaly detection with the proposed PPC method has a linear time complexity due to the deep learning approach. This allows for scalability to large datasets. While training the PPC pipeline can be computationally expensive compared to non-neural network approaches, the models used in our experiments are remarkably lightweight compared to other deep neural network architectures. The models used in sections 4.2, 4.3, and 4.4 have  $5.8 \cdot 10^5$ ,  $2.3 \cdot 10^5$  and  $9.5 \cdot 10^5$  trainable parameters, respectively, while modern deep neural networks have significantly more parameters. For example, Inceptionv3 (Szegedy, Vanhoucke, Ioffe, Shlens, & Wojna, 2016), ResNet-50 (He, Zhang, Ren, & Sun, 2016), and VGG-16 (Simonyan & Zisserman, 2014) have about  $2.4 \cdot 10^7$ ,  $2.5 \cdot 10^7$ , and  $1.4 \cdot 10^8$  trainable parameters, respectively. Furthermore, where other methods may fail to provide meaningful or intuitive anomaly scores, PPC is able to provide an anomaly score that is not only normalized to a closed unit interval  $[0, 1]$ , but also indicates a probability of data conforming to what was expected.

With our first experiment (section 4.1), we have shown that the architectural prior within this pipeline, combined with MLE loss optimization, leads to an estimation of the latent space representation likelihoods that is proportional to the underlying data distribution. This forms a solid basis for the statistical meaning of the probability of conformance. The other experiments have shown that the pipeline can be applied to several synthetic and real-world problems with different data modalities. The *sine wave frequency deviation* experiment (section 4.2) shows excellent performance for anomaly detection in a univariate time series problem. The *counting with MNIST digits* example (section 4.3) showed how the pipeline can discover sequential patterns in image data.

The *artifact detection for MRSI* experiment (section 4.4) shows the real-world application of the method to MRSI data. The probability of conformance delivers a valuable measure for the quality of MRSI spectra and enables the filtering of artifact-ridden spectra by setting a specific threshold. This is particularly useful with high-resolution whole-brain acquisition techniques where hundreds of thousands of spectra are acquired while only good-quality spectra can be quantified reliably (Maudsley et al., 2006; Nam et al., 2023). Note the CRLB% is only obtained after computationally intensive least-squares fitting of the spectra. In addition, having a segment-wise quality measure for each spectrum can allow metabolite-targeted filtering to improve studies of specific brain pathologies (Bogner, Otazo, & Henning, 2021; Govindaraju et al., 2004; Pelletier et al., 2002).

Despite the promising results, our proposed method and the experiments have some limitations. The application of the pipeline on a specific problem requires the choice of a suitable encoder-decoder pair, not only to handle the specific data type but also to handle the context of the problem. For example, in the case of the sine

wave example, it would be obvious to choose a segment length such that the receptive field of the encoder covers the largest wave period (2 seconds). Furthermore, a suitable latent space encoding dimension  $N_e$  needs to be chosen, as to prevent both under- and overfitting. While choosing a suitable encoder/decoder may not be trivial, as a rule of thumb, we suggest adopting architectures that would yield reasonably low reconstruction losses in an autoencoder application. This would guarantee the inference of information-rich latent space representations that can be used for predictive modeling.

The dependency on the decoder to regularize the model and prevent the pipeline from becoming underdetermined is necessary but inconvenient. As the predictive modeling competes with the reconstruction modeling in a joint loss landscape, the latent space representations are not fully optimized for the predictive modeling, inevitably leading to diminished performance on anomaly detection. For future research, we suggest exploring the use of contrastive learning in either a semi-supervised setting (positive and negative samples both from non-anomalous data) or a fully supervised setting (positive samples from non-anomalous data, negative samples from normal and abnormal data). We expect that the use of contrastive learning conditions the latent space such that regularization with a decoder is no longer necessary, as contrastive learning incentivizes distinct latent space representations by design.

Lastly, we recognize the lack of benchmark evaluations in this work. The lack of available real-world datasets forms an obstacle to the development and testing of CPD and AD methods (Pang et al., 2022). Publicly accessible datasets in the field of CPD and AD are either low-complexity univariate time series, outdated, or unannotated. It is therefore no surprise that the review of Nassif, Talib, Nasir, and Dakalbab (2021) shows the use of a plethora of different datasets in different works, for which a significant part of them is synthetic or simulated.

## 6 Conclusion

This study introduces a novel pipeline for anomalous change point detection that leverages an architectural prior with probabilistic predictions and latent space encoding, and a training method that captures the underlying data distributions. These distributions can then be used to determine an anomaly score in the form of a *probability of conformance*.

Theoretically, this pipeline allows for wide application to different problems and data types. Where classical methods are generally not capable of dealing with highly complex data, and deep anomaly detection methods generally lack interpretability, meaningful anomaly scores, or low computational complexity, the proposed method solves these problems.

Through a series of experiments, we evaluated the effectiveness and versatility of our proposed method across various data modalities, including synthetic time series, image data, and real-world magnetic resonance spectroscopic imaging (MRSI) data. Our findings suggest that the pipeline is capable of accurately detecting anomalous change points in different problems with different types of data, showcasing its potential for a wide range of applications in anomaly detection and monitoring.

Despite the promising results, it is important to acknowledge the limitations of our approach, including the assumptions of data normality and the dependence on specific encoder-decoder architectures. Additionally, the lack of publicly available benchmark datasets poses a challenge for comprehensive evaluation and comparison with existing methods. Future research directions include exploring contrastive learning to alleviate the dependency on decoder regularization.

In summary, our study contributes to the growing body of research in anomaly detection by presenting a widely applicable pipeline that demonstrates promising performance across diverse data domains.

## 7 Statements and declarations

**Author contributions:** All authors contributed to the study conception and design. Theoretical development was performed by Roelof G. Hup. Experimental design and execution were performed by Roelof G. Hup and Julian P. Merkofer. Data acquisition and analysis were performed by Roelof G. Hup, Julian P. Merkofer, and Alex A. Bhogal. Funding was acquired by Rik Vullings, Reinder Haakma, and Ruud J.G. van Sloun. The first draft of the manuscript was written by Roelof G. Hup and Julian P. Merkofer and all authors commented on previous versions of the manuscript. All authors read and approved the final manuscript.

**Funding:** This work is financed by the PPP Allowance made available by Top Sector Life Sciences & Health to the Dutch Heart Foundation to stimulate public-private partnerships, grant number 01-003-2021-B005, Philips Electronics Nederland B.V., and Spectralligence (EUREKA IA Call, ITEA4 project 20209).

**Competing interests:** Reinder Haakma is employed at Philips Electronics Nederland B.V.

**Ethical approval:** In-vivo spectra were extracted from the database reported in [Bhogal et al. \(2020\)](#) as part of a study approved by the medical research ethics committee of the University Medical Center Utrecht. Experiments were conducted according to the regulations of the Dutch *Medical Research Involving Human Subjects Act* and in concordance with the Declaration of Helsinki. The International Conference on Harmonization Good Clinical Practice (ICH-GCP) was used as guidance throughout all study-related activities. All participants provided written informed consent.

**Data availability:** The synthetic data used in sections [4.1](#), [4.2](#), and [4.4](#) can be generated on demand or are available upon request. The MNIST dataset in section [4.3](#) is publicly available. The in-vivo MRSI data in section [4.4](#) can be made available upon submission of a project outline to co-author Alex A. Bhogal.

## References

Apostol, E.-S., Truică, C.-O., Pop, F., Esposito, C. (2021, 6). Change Point Enhanced Anomaly Detection for IoT Time Series Data. *Water*, 13(12), 1633, <https://>

- Aryal, S., Santosh, K., Dazeley, R. (2021, 4). usfAD: a robust anomaly detector based on unsupervised stochastic forest. *International Journal of Machine Learning and Cybernetics*, 12(4), 1137–1150, <https://doi.org/10.1007/s13042-020-01225-0>
- Aryal, S., Ting, K.M., Haffari, G. (2016). Revisiting Attribute Independence Assumption in Probabilistic Unsupervised Anomaly Detection. M. Chau, G.A. Wang, & H. Chen (Eds.), (Vol. 9650, pp. 73–86). Cham: Springer International Publishing.
- Bhogal, A.A., Broeders, T.A.A., Morsinkhof, L., Edens, M., Nassirpour, S., Chang, P., ... Wijnen, J.P. (2020, 12). Lipid-suppressed and tissue-fraction corrected metabolic distributions in human central brain structures using 2D 1H magnetic resonance spectroscopic imaging at 7 T. *Brain and Behavior*, 10(12), , <https://doi.org/10.1002/brb3.1852>
- Bogner, W., Otazo, R., Henning, A. (2021, 5). Accelerated MR spectroscopic imaging—a review of current and emerging techniques. *NMR in Biomedicine*, 34(5), , <https://doi.org/10.1002/nbm.4314>
- Breunig, M.M., Kriegel, H.-P., Ng, R.T., Sander, J. (2000, 5). LOF: Identifying Density-Based Local Outliers. *Proceedings of the 2000 acm sigmod international conference on management of data* (pp. 93–104). New York, NY, USA: ACM.
- Campello, R.J.G.B., Moulavi, D., Zimek, A., Sander, J. (2015, 7). Hierarchical Density Estimates for Data Clustering, Visualization, and Outlier Detection. *ACM Transactions on Knowledge Discovery from Data*, 10(1), 1–51, <https://doi.org/10.1145/2733381>
- Chen, T., Tang, L.-A., Sun, Y., Chen, Z., Zhang, K. (2016). Entity Embedding-Based Anomaly Detection for Heterogeneous Categorical Events. *Proceedings of the twenty-fifth international joint conference on artificial intelligence (ijcai)* (pp. 1396–1403).
- De Graaf, R.A. (2019). *In vivo NMR spectroscopy: principles and techniques* (3rd ed ed.). Hoboken, NJ: John Wiley & Sons, Inc.
- Doersch, C. (2016, 6). Tutorial on Variational Autoencoders. *arXiv*, ,

- Duong, H.-T., Le, V.-T., Hoang, V.T. (2023, 5). Deep Learning-Based Anomaly Detection in Video Surveillance: A Survey. *Sensors*, 23(11), 5024, <https://doi.org/10.3390/s23115024>
- Elnaggar, R., Chakrabarty, K., Tahoori, M.B. (2019, 12). Hardware Trojan Detection Using Change-point-Based Anomaly Detection Techniques. *IEEE Transactions on Very Large Scale Integration (VLSI) Systems*, 27(12), 2706–2719, <https://doi.org/10.1109/TVLSI.2019.2925807>
- Fahim, M., & Sillitti, A. (2019). Anomaly Detection, Analysis and Prediction Techniques in IoT Environment: A Systematic Literature Review. *IEEE Access*, 7, 81664–81681, <https://doi.org/10.1109/ACCESS.2019.2921912>
- Fan, H., Zaïane, O.R., Foss, A., Wu, J. (2009, 4). Resolution-based outlier factor: detecting the top-n most outlying data points in engineering data. *Knowledge and Information Systems*, 19(1), 31–51, <https://doi.org/10.1007/s10115-008-0145-3>
- Gebski, M., & Wong, R.K. (2007). An Efficient Histogram Method for Outlier Detection. *Advances in databases: Concepts, systems and applications* (pp. 176–187). Berlin, Heidelberg: Springer Berlin Heidelberg.
- Goodfellow, I., Bengio, Y., Courville, A. (2016). *Deep Learning*. The MIT Press.
- Govindaraju, V., Gauger, G.E., Manley, G.T., Ebel, A., Meeker, M., Maudsley, A.A. (2004, 5). Volumetric proton spectroscopic imaging of mild traumatic brain injury. *AJNR. American journal of neuroradiology*, 25(5), 730–7,
- Grubbs, F.E. (1969, 2). Procedures for Detecting Outlying Observations in Samples. *Technometrics*, 11(1), 1–21, <https://doi.org/10.1080/00401706.1969.10490657>
- Gurbani, S.S., Schreibmann, E., Maudsley, A.A., Cordova, J.S., Soher, B.J., Poptani, H., ... Cooper, L.A.D. (2018, 11). A convolutional neural network to filter artifacts in spectroscopic MRI. *Magnetic Resonance in Medicine*, 80(5), 1765–1775, <https://doi.org/10.1002/mrm.27166>
- He, K., Zhang, X., Ren, S., Sun, J. (2016, 6). Deep Residual Learning for Image Recognition. *2016 IEEE conference on computer vision and pattern recognition (cvpr)* (pp. 770–778). IEEE.



- Hilal, W., Gadsden, S.A., Yawney, J. (2022, 5). Financial Fraud: A Review of Anomaly Detection Techniques and Recent Advances. *Expert Systems with Applications*, 193, 116429, <https://doi.org/10.1016/j.eswa.2021.116429>
- Huijben, I.A.M., Kool, W., Paulus, M.B., van Sloun, R.J.G. (2023, 2). A Review of the Gumbel-max Trick and its Extensions for Discrete Stochasticity in Machine Learning. *IEEE Transactions on Pattern Analysis and Machine Intelligence*, 45(2), 1353–1371, <https://doi.org/10.1109/TPAMI.2022.3157042> Retrieved from <https://ieeexplore.ieee.org/document/9729603/>
- Jang, E., Gu, S., Poole, B. (2017, 11). Categorical Reparameterization with Gumbel-Softmax. *International conference on learning representations*.
- Jang, J., Lee, H.H., Park, J.-A., Kim, H. (2021, 4). Unsupervised anomaly detection using generative adversarial networks in 1H-MRS of the brain. *Journal of Magnetic Resonance*, 325, 106936, <https://doi.org/10.1016/j.jmr.2021.106936>
- Jiang, M., Tseng, S., Su, C. (2001, 5). Two-phase clustering process for outliers detection. *Pattern Recognition Letters*, 22(6-7), 691–700, [https://doi.org/10.1016/S0167-8655\(00\)00131-8](https://doi.org/10.1016/S0167-8655(00)00131-8)
- Jiang, S.-y., & An, Q.-b. (2008, 10). Clustering-Based Outlier Detection Method. *2008 fifth international conference on fuzzy systems and knowledge discovery* (Vol. 2, pp. 429–433). IEEE.
- Knorr, E.M., Ng, R.T., Tucakov, V. (2000, 2). Distance-based outliers: algorithms and applications. *The VLDB Journal The International Journal on Very Large Data Bases*, 8(3-4), 237–253, <https://doi.org/10.1007/s007780050006>
- Kreis, R. (2004, 10). Issues of spectral quality in clinical 1H-magnetic resonance spectroscopy and a gallery of artifacts. *NMR in Biomedicine*, 17(6), 361–381, <https://doi.org/10.1002/nbm.891>
- Kreis, R., Boer, V., Choi, I., Cudalbu, C., de Graaf, R.A., Gasparovic, C., . . . Bogner, W. (2021, 5). Terminology and concepts for the characterization of in vivo MR spectroscopy methods and MR spectra: Background and experts' consensus recommendations. *NMR in Biomedicine*, 34(5), , <https://doi.org/10.1002/nbm.4347>

- Kriegel, H.-P., Kröger, P., Schubert, E., Zimek, A. (2009). Outlier Detection in Axis-Parallel Subspaces of High Dimensional Data. (pp. 831–838).
- Kyathanahally, S.P., Mocioiu, V., Pedrosa de Barros, N., Slotboom, J., Wright, A.J., Julià-Sapé, M., ... Kreis, R. (2018, 5). Quality of clinical brain tumor MR spectra judged by humans and machine learning tools. *Magnetic Resonance in Medicine*, 79(5), 2500–2510, <https://doi.org/10.1002/mrm.26948>
- Landheer, K., & Juchem, C. (2021, 7). Are Cramér-Rao lower bounds an accurate estimate for standard deviations in in vivo magnetic resonance spectroscopy? *NMR in Biomedicine*, 34(7), , <https://doi.org/10.1002/nbm.4521>
- Lecun, Y., Bottou, L., Bengio, Y., Haffner, P. (1998). Gradient-based learning applied to document recognition. *Proceedings of the IEEE*, 86(11), 2278–2324, <https://doi.org/10.1109/5.726791>
- Lin, S., Clark, R., Birke, R., Schonborn, S., Trigoni, N., Roberts, S. (2020, 5). Anomaly Detection for Time Series Using VAE-LSTM Hybrid Model. *Icassp 2020 - 2020 IEEE International Conference on Acoustics, Speech and Signal Processing (ICASSP)* (pp. 4322–4326). IEEE. Retrieved from <https://ieeexplore.ieee.org/document/9053558/>
- Liu, F., Yu, Y., Song, P., Fan, Y., Tong, X. (2020, 9). Scalable KDE-based top-n local outlier detection over large-scale data streams. *Knowledge-Based Systems*, 204, 106186, <https://doi.org/10.1016/j.knosys.2020.106186>
- Liu, F.T., Ting, K.M., Zhou, Z.-H. (2012, 3). Isolation-Based Anomaly Detection. *ACM Transactions on Knowledge Discovery from Data*, 6(1), 1–39, <https://doi.org/10.1145/2133360.2133363>
- Maudsley, A.A., Andronesi, O.C., Barker, P.B., Bizzi, A., Bogner, W., Henning, A., ... Soher, B.J. (2021, 5). Advanced magnetic resonance spectroscopic neuroimaging: Experts' consensus recommendations. *NMR in Biomedicine*, 34(5), , <https://doi.org/10.1002/nbm.4309>
- Maudsley, A.A., Darkazanli, A., Alger, J.R., Hall, L.O., Schuff, N., Studholme, C., ... Zhu, X. (2006, 6). Comprehensive processing, display and analysis for in vivo MR spectroscopic imaging. *NMR in Biomedicine*, 19(4), 492–503, <https://doi.org/10.1002/nbm.1025>

- Nam, K.M., Gursan, A., Bhogal, A.A., Wijnen, J.P., Klomp, D.W.J., Prompers, J.J., Hendriks, A.D. (2023, 9). Deuterium echo-planar spectroscopic imaging (EPSI) in the human liver in vivo at 7 T. *Magnetic Resonance in Medicine*, 90(3), 863–874, <https://doi.org/10.1002/mrm.29696>
- Nassif, A.B., Talib, M.A., Nasir, Q., Dakalbab, F.M. (2021). Machine Learning for Anomaly Detection: A Systematic Review. *IEEE Access*, 9, 78658–78700, <https://doi.org/10.1109/ACCESS.2021.3083060>
- Near, J., Harris, A.D., Juchem, C., Kreis, R., Marjańska, M., Öz, G., . . . Gasparovic, C. (2021, 5). Preprocessing, analysis and quantification in single-voxel magnetic resonance spectroscopy: experts’ consensus recommendations. *NMR in Biomedicine*, 34(5), , <https://doi.org/10.1002/nbm.4257>
- Nix, D., & Weigend, A. (1994). Estimating the mean and variance of the target probability distribution. *Proceedings of 1994 ieee international conference on neural networks (icnn'94)* (Vol. 1, pp. 55–60). IEEE.
- Oh, M.-h., & Iyengar, G. (2019, 7). Sequential Anomaly Detection using Inverse Reinforcement Learning. *Proceedings of the 25th acm sigkdd international conference on knowledge discovery & data mining* (pp. 1480–1490). New York, NY, USA: ACM.
- Oord, A.v.d., Li, Y., Vinyals, O. (2018, 7). Representation Learning with Contrastive Predictive Coding. *arXiv*, ,
- Öz, G., Alger, J.R., Barker, P.B., Bartha, R., Bizzi, A., Boesch, C., . . . Kauppinen, R.A. (2014, 3). Clinical Proton MR Spectroscopy in Central Nervous System Disorders. *Radiology*, 270(3), 658–679, <https://doi.org/10.1148/radiol.13130531>
- Pang, G., Shen, C., Cao, L., Hengel, A.V.D. (2022, 3). Deep Learning for Anomaly Detection. *ACM Computing Surveys*, 54(2), 1–38, <https://doi.org/10.1145/3439950>
- Pang, G., Ting, K.M., Albrecht, D. (2015, 11). LeSiNN: Detecting Anomalies by Identifying Least Similar Nearest Neighbours. *2015 ieee international conference on data mining workshop (icdmw)* (pp. 623–630). IEEE.

- Pang, G., Ting, K.M., Albrecht, D., Jin, H. (2016, 12). ZERO++: Harnessing the Power of Zero Appearances to Detect Anomalies in Large-Scale Data Sets. *Journal of Artificial Intelligence Research*, 57, 593–620, <https://doi.org/10.1613/jair.5228>
- Pedrosa de Barros, N., McKinley, R., Wiest, R., Slotboom, J. (2017, 12). Improving labeling efficiency in automatic quality control of MRSI data. *Magnetic Resonance in Medicine*, 78(6), 2399–2405, <https://doi.org/10.1002/mrm.26618>
- Pelletier, D., Nelson, S., Grenier, D., Lu, Y., Genain, C., Goodkin, D. (2002, 10). 3-D echo planar 1HMRS imaging in MS: metabolite comparison from supratentorial vs. central brain. *Magnetic Resonance Imaging*, 20(8), 599–606, [https://doi.org/10.1016/S0730-725X\(02\)00533-7](https://doi.org/10.1016/S0730-725X(02)00533-7)
- Posse, S., Otazo, R., Dager, S.R., Alger, J. (2013, 6). MR spectroscopic imaging: Principles and recent advances. *Journal of Magnetic Resonance Imaging*, 37(6), 1301–1325, <https://doi.org/10.1002/jmri.23945>
- Provencher, S.W. (1993, 12). Estimation of metabolite concentrations from localized in vivo proton NMR spectra. *Magnetic Resonance in Medicine*, 30(6), 672–679, <https://doi.org/10.1002/mrm.1910300604>
- Radovanovic, M., Nanopoulos, A., Ivanovic, M. (2015, 5). Reverse Nearest Neighbors in Unsupervised Distance-Based Outlier Detection. *IEEE Transactions on Knowledge and Data Engineering*, 27(5), 1369–1382, <https://doi.org/10.1109/TKDE.2014.2365790>
- Sabokrou, M., Khalooei, M., Fathy, M., Adeli, E. (2018, 6). Adversarially Learned One-Class Classifier for Novelty Detection. *2018 IEEE/CVF Conference on Computer Vision and Pattern Recognition* (pp. 3379–3388). IEEE.
- Samariya, D., & Thakkar, A. (2023, 6). A Comprehensive Survey of Anomaly Detection Algorithms. *Annals of Data Science*, 10(3), 829–850, <https://doi.org/10.1007/s40745-021-00362-9>
- Schlegl, T., Seeböck, P., Waldstein, S.M., Langs, G., Schmidt-Erfurth, U. (2019, 5). f-AnoGAN: Fast unsupervised anomaly detection with generative adversarial networks. *Medical Image Analysis*, 54, 30–44, <https://doi.org/10.1016/j.media.2019.01.010>

- Simonyan, K., & Zisserman, A. (2014, 9). Very Deep Convolutional Networks for Large-Scale Image Recognition. *ICLR*, ,
- Sluijterman, L., Cator, E., Heskes, T. (2023, 2). Optimal Training of Mean Variance Estimation Neural Networks. *arXiv*, ,
- Szegedy, C., Vanhoucke, V., Ioffe, S., Shlens, J., Wojna, Z. (2016, 6). Rethinking the Inception Architecture for Computer Vision. *2016 IEEE Conference on Computer Vision and Pattern Recognition (CVPR)* (pp. 2818–2826). IEEE.
- Tenenboim-Chekina, L., Rokach, L., Shapira, B. (2013). Ensemble of Feature Chains for Anomaly Detection. *Lncs* (Vol. 7872, pp. 295–306).
- Theiler, J., & Perkins, S. (2006). Proposed framework for anomalous change detection. *ICML Workshop on Machine Learning Algorithms for Surveillance and Event Detection* (pp. 7–14).
- van de Sande, D.M.J., Merkofer, J.P., Amirrajab, S., Veta, M., van Sloun, R.J.G., Versluis, M.J., ... Breeuwer, M. (2023, 10). A review of machine learning applications for the proton MR spectroscopy workflow. *Magnetic Resonance in Medicine*, *90*(4), 1253–1270, <https://doi.org/10.1002/mrm.29793>
- Wang, H., Pang, G., Shen, C., Ma, C. (2020). Unsupervised Representation Learning by Predicting Random Distances. *Proceedings of the twenty-ninth international joint conference on artificial intelligence (ijcai-20)* (pp. 2950–2956).
- Wu, P., Liu, J., Shen, F. (2019, 7). A Deep One-Class Neural Network for Anomalous Event Detection in Complex Scenes. *IEEE Transactions on Neural Networks and Learning Systems*, *31*(7), 1–14, <https://doi.org/10.1109/TNNLS.2019.2933554>
- Yang, X., Deng, C., Zheng, F., Yan, J., Liu, W. (2019, 6). Deep Spectral Clustering Using Dual Autoencoder Network. *2019 IEEE/CVF Conference on Computer Vision and Pattern Recognition (CVPR)* (pp. 4061–4070). IEEE.
- Yang, Z., Liu, X., Li, T., Wu, D., Wang, J., Zhao, Y., Han, H. (2022, 5). A systematic literature review of methods and datasets for anomaly-based network intrusion detection. *Computers & Security*, *116*, 102675, <https://doi.org/10.1016/j.cose.2022.102675>
- Ye, M., Peng, X., Gan, W., Wu, W., Qiao, Y. (2019, 10). AnoPCN: Video Anomaly Detection via Deep Predictive Coding Network. *Proceedings of the 27th ACM international conference on multimedia* (pp. 1805–1813). New York, NY, USA:

ACM.

Ye, N., & Chen, Q. (2001, 3). An anomaly detection technique based on a chi-square statistic for detecting intrusions into information systems. *Quality and Reliability Engineering International*, 17(2), 105–112, <https://doi.org/10.1002/qre.392>

Zhang, Y., An, L., Shen, J. (2017, 8). Fast computation of full density matrix of multispin systems for spatially localized in vivo magnetic resonance spectroscopy. *Medical Physics*, 44(8), 4169–4178, <https://doi.org/10.1002/mp.12375>